Rare Metal Materials and Engineering
Volume 55, Issue 6, June 2026
Available online at www.rmme.ac.cn

Science Press

Cite this article as: Wang Shuangjian, Wang Kelu, Lu Cuiyuan, et al. Study on Flow Stress Constitutive Relationship of GH738 Superalloy Based on Machine Learning[J]. Rare Metal Materials and Engineering, 2026, 55(06): 1437-1450. DOI: https://doi.org/10.12442/j.issn.1002-185X.20250193.

ARTICLE

Study on Flow Stress Constitutive Relationship of GH738 Superalloy Based on Machine Learning

Wang Shuangjian[1], Wang Kelu[1], Lu Cuiyuan[2], Luo Baile[1], Xu Bing[3], Zhou Shixin[3], Wang Panzhi[3]

[1] School of Aeronautical Manufacturing Engineering, Nanchang Hangkong University, Nanchang 330063, China; [2] School of Advanced Manufacturing, Nanchang University, Nanchang 330031, China; [3] Guizhou Hangyu Technology Development Co., Ltd, Guizhou 550081, China

Abstract: Hot compression experiments were conducted on GH738 superalloy using Gleeble 3500 thermal simulation machine at deformation temperature of 980–1100 °C and strain rate of 0.001–0.1 s^{-1} to study the flow stress behavior of the alloy. Three machine learning algorithms, namely random forest (RF), support vector machine (SVM), and genetic algorithm-back propagation (GA-BP) neural networks, were employed to establish constitutive relationship models for the flow stress behavior of GH738 superalloy. Subsequently, these models were compared and analyzed in terms of their predictive accuracy. The results indicate that the flow stress of GH738 superalloy decreases with the increase in deformation temperature and the decrease in strain rate. The correlation coefficients for the RF, SVM, and GA-BP constitutive relationship models are determined as 0.921, 0.998, and 0.999, while the average absolute relative errors as 14.587%, 2.112%, and 0.901%, respectively. The results demonstrate that SVM and GA-BP constitutive relationship models have better prediction accuracy than RF model in predicting the flow stress behavior of GH738 superalloy. It can provide a theoretical basis for the calculation of deformation resistance and forging tonnage under different deformation conditions, and it can also provide reliable flow stress data for numerical simulation of forging process.

Key words: GH738 superalloy; constitutive relationship model; random forest; support vector machine; GA-BP network

1 Introduction

Nickel-based superalloys exhibit outstanding comprehensive mechanical properties, as well as good oxidation and corrosion resistance, making them widely used in high-temperature bearing components of aeroengines and gas turbines[1–2]. GH738 is a γ' phase-reinforced nickel-based superalloy with excellent strength and toughness matching. It demonstrates high resistance to gas corrosion and fatigue, along with a stable structure, presenting broad application prospects in engine rotating parts[3–4]. However, the alloy has a narrow deformation temperature range, exhibits high deformation resistance, and shows a complex dynamic response to the flow behavior under varying deformation process parameters, making it a typical difficult-to-deform material[5–6]. The study of flow stress behavior during hot deformation of metals and alloys has garnered considerable attention. Accurate comprehension of flow stress behavior not only provides a theoretical basis for formulating hot working technique, but also aids in controlling the microstructure of alloys. Currently, the design and optimization of material forming processes increasingly rely on numerical simulation, while the reliability of numerical simulation results largely hinges on the constitutive relationship model. Therefore, precise modeling of flow stress behavior holds important theoretical significance and practical application value.

Currently, the most commonly used constitutive relationship models are phenomenological and physical models[7–8]. Phenomenological models encompass the Arrhenius model, Johnson-Cook model, and Fields-Backofen model. These

Received date: June 17, 2025
Foundation item: Natural Science Foundation of Jiangxi Province (20232BAB214001); Innovation Fund for Fostering Young Talents of Nanchang University (PYQN20230077); 2023 Ganpo Talents Support Program-High Level and Urgently Needed Oversea Talents Program (20232BCJ25074)
Corresponding author: Wang Kelu, Ph. D., Professor, School of Aeronautical Manufacturing Engineering, Nanchang Hangkong University, Nanchang 330063, P. R. China, E-mail: wangkelu@126.com

models determine material constants through regression analysis and establish a flow stress constitutive relationship model that takes into account deformation temperature, strain rate, and strain[9–10]. However, phenomenological models often overlook the internal relationship between flow stress and influencing factors, leading to generally weak extrapolation ability. In contrast to phenomenological models, physical models are based on thermodynamic theory, heat-activated dislocation motion, and slip dynamics, and they establish a constitutive relationship model starting from microstructural features, such as dislocation density and grain size. Nevertheless, obtaining the physical parameters of materials is challenging and imposes certain restrictions on its establishment and use[11–12]. Additionally, the dynamic response behavior, deformation mechanism, and flow characteristics in thermoplastic deformation processes are highly complex. Thus, the traditional phenomenological or physical model entails significant workload while struggling to ensure accurate prediction of flow stress. Therefore, it is necessary to seek a more accurate method for constructing constitutive relationship models[13–14]. Machine learning (ML) can autonomously capture complex nonlinear relationships, which overcomes shortcomings of traditional regression methods, providing guarantee for multi-field coupling modeling of constitutive relationships as well as accurate prediction of flow stress[15–16]. Ding et al[17] investigated the thermal deformation behavior of TC18 alloy at temperatures ranging from 993 K to 1113 K and strain rate ranging from 0.001 s^{-1} to 1 s^{-1}. A ML model describing the thermoplastic constitutive relationship of alloys was established by random forest (RF), support vector regression (SVR), backpropagation artificial neural network (BPANN), and Gaussian process regression (GPR). The results show that the predictive abilities of the four established ML models are GPR>BPANN>RF>SVR. Xiao et al[18] obtained the stress-strain curve of Ti-5Al-5Mo-5V-1Cr-1Fe alloy through Gleeble thermal simulation experiments. According to the stress-strain curve, the constitutive models were established by the Arrhenius equation and BPANN. The constitutive model constructed by BPANN has higher fitting accuracy, with the Pearson ' s correlation coefficient (R) of 0.999 02 and mean absolute percentage error (MAPE) of 5.499 %. Poluru et al[19] analyzed the mechanical responses of 92W-5Co-3Ni alloy when the dynamic strain rate was 1800 – 4200 s^{-1} and the temperature was at 323–873 K. The Arrhenius constitutive model and ML-based RF model were developed to predict flow stress. The Arrhenius model accurately predicts the flow stress behavior with a correlation coefficient (R) of 0.9766 and an average absolute relative error (AARE) of 2.033%. However, RF model demonstrates the best prediction of flow stress behavior with an R of 0.9912 and an AARE of 1.145%. Qiao et al[20] studied the hot deformation behavior of $Fe_2Ni_2CrAl_{1.2}$ multi-principle element alloys (MPEAs). Hot compression tests were conducted at various temperatures ranging from 800 ℃ to 1100 ℃ at different strain rates from 0.001 s^{-1} to 1 s^{-1}, The stress-strain curves obtained under different processing conditions were used to develop the constitutive model for the alloy. The advanced ML models, including SVR, artificial neural network (ANN), generalized regression neural network, and RF, were trained to predict the flow behavior of $Fe_2Ni_2CrAl_{1.2}$ MPEAs. The predictive capability of ML algorithms was estimated, and SVR model performed better among the developed four algorithms. Then, particle swarm optimization (PSO) was imposed to SVR model to further enhance its prediction accuracy. The developed PSO-SVR model achieved an average testing R^2 of 0.9819, as well as low root-mean-square error and MAPE values, demonstrating its strong predictive performance.

RF, SVM, and genetic algorithm-back propagation (GA-BP) neural networks are essential ML methods. RF is an ensemble learning method with decision trees as the basic model, primarily using random data selected from the dataset to construct a large number of decision trees. Each tree is constructed by randomly selecting specific attributes for each node, and their results are integrated to achieve high prediction accuracy without increasing computational complexity[21–22]. In recent years, RF has gained widespread attention due to its simplicity, accuracy, and robustness. For instance, Mcelfresh et al[23] used RF, linear regression, K-nearest neighbor, and ANN to predict and evaluate the yield strength and hardening rate of Ti-6Al-4V alloy. The results demonstrated that RF model exhibits superior predictive performance. Aghaaminiha et al[24] developed ML models using RF, ANN, and K-nearest neighbor to forecast the impact of corrosion inhibitors on corrosion rate in low-carbon steel, indicating that the trained RF model achieved the optimal prediction accuracy. However, it should be noted that decision trees used in constructing RF may suffer from low classification accuracy or high classification correlation issues, leading to a decline in predictive performance[25]. Currently, there are few reports on employing RF model for establishing material constitutive relationship.

SVM is a statistical-based ML method, which is particularly suitable for modeling tasks characterized by small datasets, high dimensionality, and risk of overfitting. In comparison to neural networks, SVM can effectively balance model complexity and learning ability with restricted sample information, demonstrating strong generalization capabilities in small sample learning[26–27]. Li et al[28] used the SVM method to analyze the impact of alloying elements on the mechanical properties of Ti-25V-15Cr flame retardant titanium alloy and to optimize alloy composition. The results indicated that SVM model exhibits fine predictive capability and can accurately reflect the quantitative relationship between alloying elements and mechanical properties. Additionally, Limbadri et al[29] developed strain compensated Arrhenius equation and SVM constitutive relationship models for Zr-4 alloy, separately, revealing better prediction accuracy with the SVM model. However, achieving optimal performance with an SVM model requires careful selection of parameters related to kernel function and regularization for improved learning and prediction accuracy[30–31]. Currently, there are few reports on using

SVM to establish constitutive relationships for superalloys.

As a significant ML approach, BP neural network has the capacity to learn and store input-output mapping relationships, while continuously adjusting network weights and thresholds through BP in order to minimize errors. Nevertheless, BP networks suffer from drawbacks, such as bloated structure, susceptibility to overfitting or falling into local minima, as well as slow convergence rates[32]. Using GA for optimizing original weights and biases within BP networks can significantly enhance model accuracy[33]. GA-BP model has been applied in predicting flow stress behavior of alloys. For instance, Chu et al[34] established constitutive relationship models for Zr-4 alloy using both conventional BP network and GA-BP network. The results show that the GA-BP network exhibits superior prediction accuracy, with an error within ±2%, in contrast to approximately ±6% for the conventional BP network. Wen et al[35] constructed a GA-BP network constitutive relationship model for ultra-high strength steel, which demonstrated nice prediction accuracy with AARE of 0.2434% during training data, while reaching a correlation coefficient R of 0.9999. Test data showed an AARE of 2.4487% and a correlation coefficient R of 0.9961. Currently, there are few reports on using GA-BP networks in predicting flow stress behavior specifically for superalloys.

In this study, the thermal deformation behavior analysis of GH738 superalloy was conducted through isothermal constant strain rate compression experiments using Gleeble-3500 thermal simulation machine. RF, SVM, and GA-BP models were employed to establish the flow stress constitutive relationship. Comparison among these three constitutive relationship models was made based on correlation coefficient R, AARE, and relative error. These research findings provide theoretical guidance for calculating deformation resistance and process design during the forging of GH738 superalloy. Additionally, it provides fundamental flow stress data that is essential for numerical simulations of the forging process for this particular alloy.

2 Experiment and Modeling

2.1 Hot compression experiment

The experimental material was a GH738 superalloy forging bar, with the following chemical composition (wt%): C of 0.037, Cr of 19.44, Co of 13.53, Mo of 4.34, Ti of 2.98, Al of 1.45, Fe of 0.92, Zr of 0.08, and balanced Ni.

The isothermal compression experiment at constant strain rate was conducted using a Gleeble 3500 thermal simulator with samples of Φ8 mm×12 mm. Tantalum pieces were affixed to both ends of the sample before the hot compression experiment, and lubricant was applied to reduce the friction between the tantalum pieces and the sample. Deformation temperatures ranged from 980 °C to 1100 °C, and strain rates were set at 0.001, 0.01, and 0.1 s^{-1} with a maximum height reduction rate of about 60% (corresponding to approximately true strain of 0.92). The sample was heated at a rate of 10 ℃/s to the preset deformation temperature, then held for 300 s to ensure temperature uniformity, compressed, and finally cooled in vacuum.

2.2 ML algorithm

2.2.1 RF model

RF model is based on repeated sampling technique of self-service method. This method mainly generates a large number of decision trees by randomizing variables and data, and finally integrates the results of all decision trees, indicating that good prediction accuracy may be obtained[36]. RF method randomly selects k data from the original sample containing n samples as training samples, and the training samples are sampled k times (each sample requires replacement information) to obtain a new training set containing k training samples, which are independent of each other. Part of the input data for some of the decision trees are used as the test set[37–38]. The test set is taken as input vector $\boldsymbol{X}$ and imported into RF model to obtain prediction vectors $\{h_1(\boldsymbol{X}), h_2(\boldsymbol{X}), ..., h_k(\boldsymbol{X})\}$. Define $\boldsymbol{Y}$ as the output vector, and then calculate or draw the edge function of the predictor in RF classifier, which can be expressed as follows[21]:

$$\begin{aligned}\text{margin}(\boldsymbol{X},\boldsymbol{Y}) = &\text{av}_k I[h_k(\boldsymbol{X}) = \boldsymbol{Y}] \\ &-\max_{j \neq Y} \text{av}_k I[h_k(\boldsymbol{X}) = \boldsymbol{j}]\end{aligned} \tag{1}$$

where the function I is the objective function, av_k is the calculated average, and $\boldsymbol{j}$ is a vector misclassified into another class. The edge function represents the difference between the average weight that correctly classifies $\boldsymbol{X}$ (input vector) to $\boldsymbol{Y}$ (output vector) and the maximum weight that misclassifies $\boldsymbol{X}$ (input vector) to other class vectors in the ensemble classifier. The larger the edge function value, the better the classification reliability, and the stronger the generalization and prediction ability of the model.

If the generalization error of the whole RF is expressed as PE^*, the generalization error of a single regression tree can be expressed as follows[21]:

$$PE^* = P_{X,Y}[\text{margin}(\boldsymbol{X},\boldsymbol{Y}) < 0] \tag{2}$$

where $P_{X,Y}$ represents the probability of falling on the $(\boldsymbol{X}, \boldsymbol{Y})$ vector space.

The generalization error reflects the predictive ability of a single tree, and RF has the advantage of reducing the overall generalization error by aggregating the predicted results of multiple trees. By analyzing the generalization error of the tree, the performance of the RF model can be evaluated and optimized.

As the number of decision trees in RF model tends to be positively infinite, the generalization error corresponding to the model satisfies the convergence relation[39], as shown in Eq. (3). This convergence behavior explains the robustness of RF for high-variance features but implies restricted sensitivity to low-variance inputs, like small-strain increments.

$$\begin{aligned}\lim_{k \to \infty} PE^* = &P_{X,Y}\{[P_\theta[h(\boldsymbol{X},\boldsymbol{\theta}) = \boldsymbol{Y}] \\ &-\max_{j \neq Y} P_\theta[h(\boldsymbol{X},\boldsymbol{\theta}) = \boldsymbol{j}] < 0\}\end{aligned} \tag{3}$$

where k is the number of decision trees, $\boldsymbol{\theta}$ is a random vector, and P_θ is a distribution probability of random vector $\boldsymbol{\theta}$. In other words, the training degree of ML algorithm can be deepened by increasing the number of decision trees

indefinitely, and the fitting ability of ML algorithm can be enhanced. In this case, the prediction deviation tends to zero infinitely, and the generalization error converges to a fixed value. Therefore, entering a new sample set into RF model can also obtain a good prediction effect without overfitting[39].

2.2.2 SVM model

SVM uses hinge loss function to calculate empirical risk, and adds regularization term to the solution system to optimize structural risk. SVM can seek the best compromise between complexity (learning accuracy of specific training samples) and learning ability to recognize arbitrary samples without making mistakes, showing unique advantages in solving small samples and nonlinear and high-dimensional pattern recognition problems[40]. In the process of establishing SVM based model, given training sample set $D=\{(x_1, y_1), (x_2, y_2), ..., (x_i, y_i)\}$ and based on training set D, the model finds a partition hyperplane in the sample space to separate samples of different classes. $\boldsymbol{x}_i \in \mathbf{R}_n$ is the input variable and $\boldsymbol{y}_i \in \mathbf{R}$ is the output variable. The input vector can be mapped from the original feature space to the high-dimension Hilbert space by the nonlinear function, and the nonlinear problem can be transformed into a linearly separable problem[41]. Thus, the optimal regression function $f(x)=\omega\varphi(x)+b$ can be obtained. According to the principle of structural risk minimization, the objective function and constraint conditions are set as follows[42]:

$$\begin{cases} \min\limits_{\omega,b,e} J(\omega,b,e) = \dfrac{1}{2}\omega^{\mathrm{T}}\omega + \dfrac{1}{2}\gamma\sum_{i=1}^{N} e_i^{\,2} \\ \text{s.t.} y_i = \omega^{\mathrm{T}}\varphi(x_i) + b + e_i \quad i = 1, 2, 3, ..., n \end{cases} \tag{4}$$

where $J(\omega, b, e)$ is the optimization function of the objective function φ; ω is the space weight coefficient; γ is the penalty coefficient of the loss function, and $\gamma \geqslant 0$; b is the deviation; e is the training error; e_i is the training error of the ith data.

Lagrange function (L) is introduced to optimize the objective function in the formula into the solution of dual space[43]:

$$L(\omega,b,e,a) = J(\omega,b,e) - \sum_{i=1}^{l}\left[a_i\omega^T\varphi(x_i) + b + e_i - y_i\right] \tag{5}$$

where a is the Lagrange multiplier; a_i is the Lagrange multiplier of the ith data.

Based on the optimization theory, the partial derivatives of ω, b, e_i, and a_i are obtained according to the Lagrange function:

$$\begin{cases} \dfrac{\partial L}{\partial a_i} = 0 \rightarrow \omega^{\mathrm{T}}\varphi(x_i) + b + e_i - y_i = 0 \quad i = 1, 2, 3, ..., n \\ \dfrac{\partial L}{\partial e_i} = 0 \rightarrow a_i = \gamma e_i \quad i = 1, 2, 3, ..., n \\ \dfrac{\partial L}{\partial b} = 0 \rightarrow \sum_{i=1}^{l} a_i = 0 \\ \dfrac{\partial L}{\partial \omega} = 0 \rightarrow \omega = \sum_{i=1}^{l} a_i\varphi(x_i) \end{cases} \tag{6}$$

By eliminating ω and e_i from the above equation, the linear equation is obtained:

$$\begin{cases} \boldsymbol{s}^{\mathrm{T}}\boldsymbol{a} = 0 \\ \boldsymbol{s}\boldsymbol{b} + (K + \gamma^{-1}\boldsymbol{I})\boldsymbol{a} = \boldsymbol{y} \end{cases} \tag{7}$$

where $\boldsymbol{y}=[y_1,y_2,...,y_l]^{\mathrm{T}}$; $\boldsymbol{I}$ is the identity matrix; $\boldsymbol{s}=[1,2,3,...,n]$; $\boldsymbol{a}=[a_1,a_2,a_3...,a_l]^{\mathrm{T}}$; $\boldsymbol{b}=[b_1,b_2,b_3...,b_l]^{\mathrm{T}}$; $K=\boldsymbol{\varphi}(x_i)^{\mathrm{T}}\boldsymbol{\varphi}(x_j)$.

According to Mercer ' s theorem[44–45], if the mapping function is known, it can be converted into radial basis function (RBF) kernel $k(x_i, y_j)$ by inner product operation, and $\boldsymbol{a}$ and $\boldsymbol{b}$ in Eq. (7) are solved by least square method. Among them, RBF kernel is as follows: $k(x_i, x_j)=\exp(-\dfrac{\left\| x_i, x_j \right\|^2}{2\delta^2})$, where δ is the parameter representing the width of the kernel function and is used to calculate the similarity between the sample data point and the support vector because of its strong nonlinear mapping ability, high fault tolerance, and insensitivity to the dimensionality of the input space.

The critical hyperparameters, penalty coefficient C and RBF kernel width γ, were optimized through exhaustive grid search[46]. The search space contained discrete values: $C \in \{0.1, 1, 10, 100\}$ and $\gamma \in \{0.001, 0.01, 0.1, 1\}$, yielding 16 parameter combinations. For each combination, the prediction performance was evaluated using AARE on the training dataset (337 samples). AARE was calculated as follows:

$$\text{AARE} = \frac{100\%}{n}\sum_{i=1}^{n}\left|\frac{P_i - E_i}{E_i}\right| \tag{8}$$

where n is the number of training samples (n=337), P_i is the predicted flow stress value, and E_i is the corresponding experimental flow stress value. Optimization identified the combination of C=10 and γ=0.01 as optimal one[17], achieving a minimal training AARE of 1.817% (indicating the smallest error among all tested combinations). Generalization capability was subsequently validated using an independent test set (338 samples).

2.2.3 GA-BP network

GA-BP network inherits the advantages of high accuracy of BP network model, and can optimize data in restricted training data. By optimizing weight (w_i), bias (b_i), and hyperparameters, GA-BP network avoids local optimization caused by randomness of initial parameters, and enhances the correlation between experimental data and predicted data. It is helpful to improve the iteration efficiency and prediction accuracy of BP network[47–48], and the schematic diagram of its process is shown in Fig.1. GA-BP network can be divided into three parts: BP network structure determination, GA-optimized network weight and threshold, and BP network training and prediction[49]. Among them, BP network needs to determine the topology structure according to the input and output parameters of the sample, and then determine the individual coding length in GA. Individuals corresponding to the optimal fitness value are obtained through GA selection, crossover, and mutation operations[50–51]. BP network uses the initial network weight and threshold value corresponding to the optimal individual optimized by GA for local search to obtain the predicted value with less error.

GA parameters were optimized via systematic sensitivity analysis. Population size was evaluated across discrete values {30, 50, 70}, with 50 yielding the optimal efficiency-accuracy balance. Crossover probability was fixed at 0.7 using arithmetic crossover, consistent with established GA practices. Mutation probability was determined as 0.07[52], implemented via non-uniform mutation with decay parameters (b=2, $G_{\max}$=1000, k=3). Termination occured when the continuous

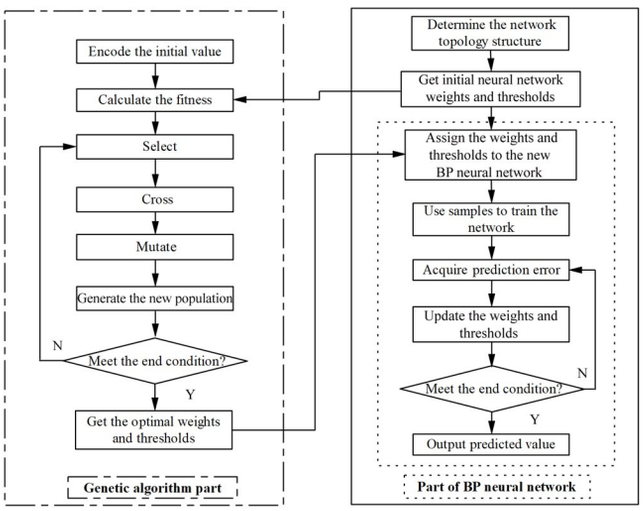

Fig.1 Flow chart of GA-BP model during training

improvement of fitness for up to 1000 generations or 50 consecutive generations was less than 0.1% to meet the goal of minimizing error[53].

GA-BP network leveraged the predictive accuracy of BP networks while mitigating restrictions, such as susceptibility to local minima and slow convergence. This was achieved by employing GA to globally optimize critical network parameters prior to gradient-based fine-tuning. Specifically, GA targeted optimization of (1) network parameters (initial connection weights w_i and neuron biases b_i), (2) learning hyperparameters (learning rate of η =0.02 and momentum coefficient of α =0.9), and (3) topology (number of hidden neurons, optimized to 6 within the range of 4–16).

Sensitivity analysis was employed to optimize parameter, as shown in Table 1. The selected population size of 50 provided optimal efficiency-accuracy trade-offs. Non-uniform mutation (b=2, probability of 0.07) maintained solution diversity, while arithmetic crossover (probability of 0.7) preserved effective solution components. Termination occurred after 1000 generations or stagnation of improvement.

This GA pre-optimization substantially enhanced convergence efficiency relative to traditional BP with random initialization: a 67% reduction in iterations (50±10 vs. 150±25). The acceleration stemmed from global search capability of GA, initializing the BP network near optimal solutions prior to gradient descent refinement. The optimized hyperparameters (η, α) further stabilized convergence by balancing exploration-exploitation trade-offs.

Following GA optimization, BP network executed local search using the genetically optimized parameters. This hierarchical approach synergized population-based global exploration with gradient-based local exploitation, enabling high-fidelity prediction of complex flow stress relationships while maintaining computational efficiency.

Table 1 GA parameters and optimized BP hyperparameters

Parameter	Value	Optimization method
Population size	50	Sensitivity analysis: {30, 50, 70}
Crossover probability	0.7	Arithmetic crossover
Mutation probability	0.07	Non-uniform mutation (b=2)
Termination criteria	Δfitness<0.1%	-
Optimized BP parameter	η=0.02, α=0.9, hidden neurons=12	-

2.3 Data pre-processing and feature engineering

2.3.1 Data standardization

To eliminate the influence of dimensional differences among input features (strain ε, strain rate $\dot{\varepsilon}$, and deformation temperature T), all features were standardized to zero mean and unit variance using Eq.(9):

$$x_{\text{std}} = \frac{x - \mu}{\sigma} \tag{9}$$

where x and x_{std} represent input features and standardized input features, respectively; μ is the mean; σ is the standard deviation of each feature[54].

2.3.2 Outlier treatment

Experimental flow stress values with standard deviations beyond ±3 from the mean were identified as outliers and removed to ensure model robustness. This resulted in the exclusion of 2.8% of the original data points (19 out of 675).

2.3.3 Feature engineering

Given the established physical significance of strain, strain rate, and temperature in constitutive modeling[1–7], no additional feature construction (e. g., polynomial terms) was applied. The input feature set remained: strain ε (dimensionless), strain rate $\dot{\varepsilon}$ (s^{-1}), and deformation temperature T (°C).

2.3.4 Data range

The ranges of input features and output labels were summarized in Table 2.

3 Results and Discussion

3.1 Flow stress behavior and deformation mechanism

Fig. 2 shows true stress-true strain curves of GH738 superalloy at different strain rates under deformation temperatures of 980, 1040, and 1100 ℃. Similar true stress-true strain curves were observed at 1010 and 1070 ℃. It can be observed that under certain conditions, such as 980 – 1100 ℃/0.001 s^{-1}, 1010–1100 ℃/0.01 s^{-1}, and 1100 ℃/0.1 s^{-1}, the true stress-true strain curves exhibit steady-state flow characteristics, while they show flow softening characteristics

Table 2 Range of input feature and output label

Parameter	Range
Strain, ε	0.05–0.92
Strain rate, $\dot{\varepsilon}$/s^{-1}	0.001–0.1
Deformation temperature, T/°C	980–1100
Flow stress, σ/MPa (label)	12.4–286.7

under other conditions, such as 980 ℃/0.01 s^{-1} and 980 – 1070 ℃/0.1 s^{-1}. In addition, it can be observed from Fig.2 that the elastic deformation stage is very short and almost invisible. This is because the elastic deformation of the alloy in the process of hot deformation is very small, so it is difficult to distinguish elastic deformation stage in the flow curve. Such phenomenon is also observed in some nickel-based superalloys, such as Waspaloy and GH99[55–58].

From Fig. 2, flow stress of GH738 superalloy decreases with the decrease in strain rate. The main reason is that the strain rate decreases, the number of dislocations formed per unit of time is reduced, and the work-hardening effect is weakened. At the same time, the slower strain rate can provide a longer period of time for the nucleation and growth of dynamic recrystallized grains, and provide favorable conditions for the dislocations slip, cross-slip, and climb. All these factors contribute to a reduction in flow stress[59–60]. In addition, the flow stress of GH738 superalloy decreases with the increase in deformation temperature. This is mainly because a higher deformation temperature promotes the occurrence of dynamic recovery and dynamic recrystallization (DRX). At the same time, the thermal activation effect is enhanced, which improves atomic diffusion, dislocation cross-slip, and grain boundary migration, thereby promoting intergranular deformation coordination and ultimately reducing the flow stress[61–62]. Some scholars have demonstrated the relationship between flow stress and temperature by analyzing the microstructure evolution characteristics of GH738 superalloy. Wang et al[63] showed that the deformation under the condition of 980 °C/1.0 s^{-1} results in elongated grains without DRX, which is consistent with high flow stresses. In contrast, at 1040 °C/1.0 s^{-1}, fully recrystallized and equiaxed fine-grains confirm DRX activation, explaining the significant stress reduction. This trend is further validated by Wang et al[63]. They demonstrated that under the condition of 1000 °C/1.0 s^{-1}, partial DRX occurs with restrict grain refinement, while complete DRX at 1150 °C/0.01 s^{-1} yields uniform equiaxed grains. The refined DRX grains at higher temperatures reduce barriers to dislocation motion, directly lowering flow stress via the Hall-Petch effect. Additionally, the absence of DRX at low temperatures (e. g., 980 °C) promotes dislocation pile-up, increasing work hardening. Conversely, DRX at elevated temperatures facilitates dislocation annihilation, enhancing thermal softening. From the point of view of reducing deformation resistance, GH738 superalloy should be forged at the high deformation temperature and slow strain rate.

To quantitatively link the observed macroscopic flow softening (e. g., at 980 °C/0.01 s^{-1}) to underlying microstructural evolution, DRX kinetics data for GH738 superalloy are incorporated. Zhou et al[58] demonstrated that within the temperature range of 980–1040 °C and strain rates of 0.01–0.1 s^{-1}, DRX fraction (X_{drex}) follows an Avrami-type kinetics model, as shown in Eq. (10).

$$X_{drex} = 1 - \exp\left[- k_d \left(\frac{\varepsilon - \varepsilon_c}{\varepsilon_p} \right)^{n_d} \right] \tag{10}$$

where ε_c and ε_p denote critical and peak strains for DRX initiation, respectively; k_d and n_d are material constants. At 980 °C/0.01 s^{-1}, ε_c and ε_p are approximately 0.12 and 0.25, respectively[58]. Concurrently, dissolution kinetics of the primary strengthening γ''-Ni_3(Nb, Mo) phase significantly contributes to flow softening. Zhou et al[57] reported via TEM and EBSD that the volume fraction of γ'' phase decreases from approximately 12% at 950 °C to below 5% above 1000 °C during deformation at $\dot{\varepsilon}$=0.01 s^{-1}, directly correlating with a 20%–25% reduction in stress contribution. Furthermore, DRX grain refinement occurs, with average grain size decreasing from initial approximately 50 μm to 8–10 μm at ε=0.6 under these conditions[55–58]. The synergistic effect of γ'' dissolution (reducing resistance to dislocation glide) and DRX nucleation/growth (resetting dislocation density) provides a mechanistic basis for the pronounced flow softening observed in Fig.2.

3.2 Establishment and verification of constitutive relationship model

3.2.1 RF model

(1) Establishment of RF model

Based on the basic principle of RF algorithm presented in Section 2.2.1, strain ε, strain rate $\dot{\varepsilon}$, and deformation temperature T of GH738 superalloy during isothermal compression experiment at constant strain rate are taken as input vector $\boldsymbol{X}$ and flow stress is taken as σ as output vector $\boldsymbol{Y}$ to establish an RF constitutive relationship model. In RF model, the prediction results generated by k decision trees (test set data) are integrated in parallel, namely the results of k test sets (y_1, y_2, ..., y_k) to find the average, and then the predicted stress

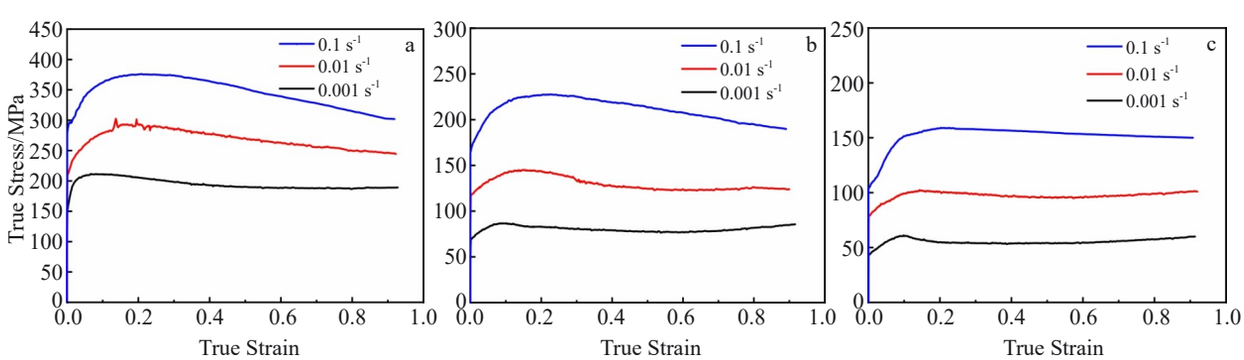

Fig.2 True stress-true strain curves of GH738 superalloy under different deformation conditions: (a) 980 ℃; (b) 1040 ℃; (c) 1100 ℃

can be obtained. Therefore, the constitutive relationship model of GH738 superalloy based on RF model can be expressed as follows[38,64]:

$$\sigma = \frac{1}{k}\sum_{i=1}^{k} y_i \tag{11}$$

where σ is the flow stress and y_i is the prediction result of the i th test set.

675 sets of flow stress data were input to the established RF model. In order to improve the generalization ability of the constitutive relationship model[65], 337 sets of data were used to train the RF model, and the remaining 338 sets of data were used to verify the prediction accuracy of the model. The nearly 1∶1 training-testing partitioning (337 training samples: 338 testing samples) was deliberately implemented to rigorously validate model generalization capability—a critical priority for industrial forging applications requiring reliable extrapolation without considering deformation conditions. This strategy aligns with emerging best practices in materials informatics, where larger test sets statistically strengthen accuracy metrics (e. g., correlation coefficient R and AARE) by mitigating sampling bias. Constitutive modeling research increasingly adopts comparable approaches, as demonstrated by Qiao et al[66] employing 50% testing for MPEAs and Poluru et al[67] allocating 45% of data for validation under extreme strain rates—ensuring methodological consistency with contemporary research paradigms.

(2) Verification of RF model

Fig. 3 shows the comparison between the flow stress predicted by RF model and the experimental values of GH738 superalloy at strain rates of 0.001 – 0.1 s^{-1} and deformation temperatures of 980, 1040, and 1100 °C. As can be seen from Fig. 3, there is a large deviation between predicted value and the experimental value on the whole, especially when the strain is small, and the prediction accuracy is lower.

In addition, correlation coefficient R and AARE can also be used to quantitatively evaluate the prediction accuracy of the constitutive relationship model. The calculation formulas of R and AARE are shown in Eq. (12) and Eq. (8), respectively[65,68].

$$R = \frac{\sum_{i=1}^{N}(P_i - \bar{P})(E_i - \bar{E})}{\sqrt{\sum_{i=1}^{N}(P_i - \bar{P})^2}\sqrt{\sum_{i=1}^{N}(E_i - \bar{E})^2}} \tag{12}$$

where P_i and E_i are the predicted value and experimental value of the ith sample, respectively; $\bar{P}$ and $\bar{E}$ are the average values of P_i and E_i, respectively; N is the number of samples.

Fig. 4 shows the correlation between the flow stress value predicted by RF model and the experimental value. Only a few data points in RF model are concentrated near the diagonal line, and the correlation coefficient R is 0.921, which indicates that the predicted value of flow stress has a general correlation with the experimental value of flow stress. By substituting the predicted value and the experimental value of flow stress into Eq. (8), AARE of 14.587% can be calculated, which indicates that the prediction accuracy of established RF model is low.

To further validate the capability of RF model, the predicted values of peak stress under various deformation conditions (temperature of 980 – 1100 °C, strain rate of 0.001 – 0.1 s^{-1}) were compared against experimental values. This quantitative comparison confirms substantial restrictions in predictive performance of RF for critical stress states, as evidenced by its accuracy metrics (R=0.964, AARE=11.335%), as shown in Fig. 5. This magnitude of error (AARE=14.587%, when considering the full constitutive behavior) notably exceeds acceptable industrial tolerances (±15%) for forging applications.

3.2.2 SVM model

(1) Establishment of SVM model

According to the basic principles of SVM algorithm presented in Section 2.2.2, the alloy constitutive relationship based on SVM model can be summarized as follows[43]:

$$y_{x_i} = \sum_{i=1}^{n} a_i \exp\left(-\frac{\left\| x_i, x_j \right\|^2}{2\delta^2}\right) + b \tag{13}$$

where n is the total number of samples; x_i is the input variable (strain ε, strain rate $\dot{\varepsilon}$, and deformation temperature T); x_j is the central variable; $\left\| x_i, x_j \right\|$ is the Euclidean distance between x_i and x_j.

The experimental parameters ε, $\dot{\varepsilon}$, and T of GH738 superalloy during isothermal compression experiment at constant strain rate were taken as input variables x_i, flow stress σ was taken as output variables y_{x_i}, and a SVM constitutive relationship model was established. 675 sets of flow stress data were input to the established SVM model. 337 sets of data were randomly selected for constitutive relationship model training, and the remaining 338 sets of data were used for model testing to verify the prediction accuracy of the model.

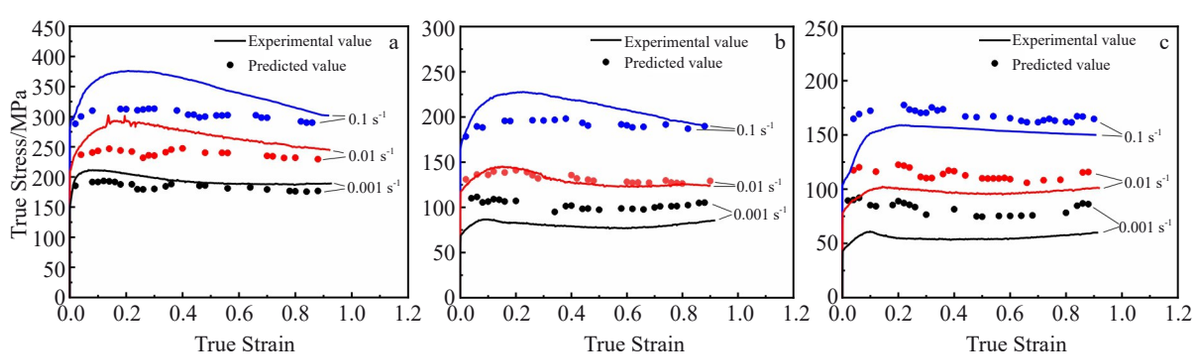

Fig.3 Comparison between true stress values predicted by RF model and the experimental values of GH738 superalloy at strain rates of 0.001–0.1 s^{-1} and different deformation temperatures: (a) 980 °C; (b) 1040 °C; (c) 1100 °C

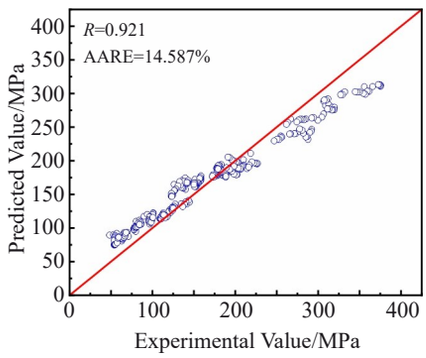

Fig.4 Correlation analysis between the flow stress values predicted by RF model and the experimental values

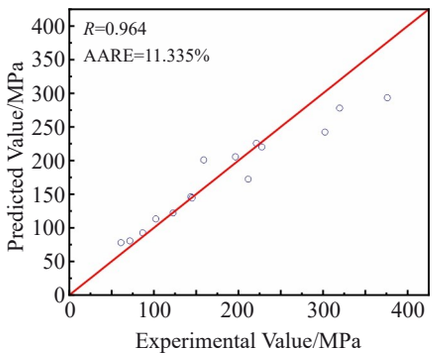

Fig.5 Correlation analysis between the peak stress values predicted by RF model and the experimental values

(2) Verification of SVM model

Fig. 6 shows the comparison between the true stress values predicted by SVM model and the experimental values of GH738 superalloy at strain rates of 0.001 – 0.1 s^{-1} and deformation temperatures of 980, 1040, and 1100 °C. As can be seen from Fig. 6, the predicted values of SVM model are mostly consistent with the experimental values. But the error of some predicted values is large, especially at the low strain stage under conditions of 980 ℃ and 0.01 s^{-1}. Comparing Fig.6 with Fig.3, it can be seen that the prediction accuracy of SVM model is significantly higher than that of RF model.

Fig.7 shows the correlation between the predicted values by SVM mode and experimental values of flow stress. SVM model has high prediction accuracy, its correlation coefficient R is 0.998, and AARE is about 2.112%.

SVM model exhibits markedly improved accuracy compared to RF model, as demonstrated in Fig. 8. Across all tested conditions (temperature of 980–1100 °C, strain rate of 0.001 – 0.1 s^{-1}), the predicted peak stress values are in close agreement with experimental values, with 80% of relative errors falling within ±5%. This high-fidelity prediction confirms robustness of SVM model for capturing key deformation features under complex thermo-mechanical conditions.

3.2.3 GA-BP model

(1) Establishment of GA-BP model

Based on the basic principle of GA-BP network presented in Section 2.2.3, GA-BP model was established with the experimental parameters of GH738 superalloy during isothermal compression experiment at constant strain rate: strain ε, strain rate $\dot{\varepsilon}$, and deformation temperature T as input variables and flow stress σ as output variables. 675 sets of flow stress data were input to the established GA-BP model. 337 sets of data were used to train the GA-BP model, and the remaining 338 sets of data were used to verify the prediction accuracy of the model. When the number of iterations of GA-BP model reaches 1000, the model reaches a satisfactory convergence level. At the same time, through cross-validation, it is found that the model is the best when the population size is 50.

(2) Verification of GA-BP model

Fig. 9 shows the comparison between the flow stress predicted by GA-BP model and the experimental values of GH738 superalloy at strain rates of 0.001 – 0.1 s^{-1} and deformation temperatures of 980, 1040, and 1100 °C. It can be seen from Fig. 9 that the predicted values of GA-BP model are in good agreement with the experimental values. Comparing Fig.9 with Fig. 6, it can be seen that the prediction accuracy of GA-BP model is significantly higher than that of SVM model.

Fig. 10 shows the correlation between the flow stress value predicted by GA-BP model and the experimental value. GA-BP model has high prediction accuracy, its correlation coefficient R is as high as 0.999, and AARE is only 0.901%.

Fig. 11 quantitatively compares peak stress value predicted

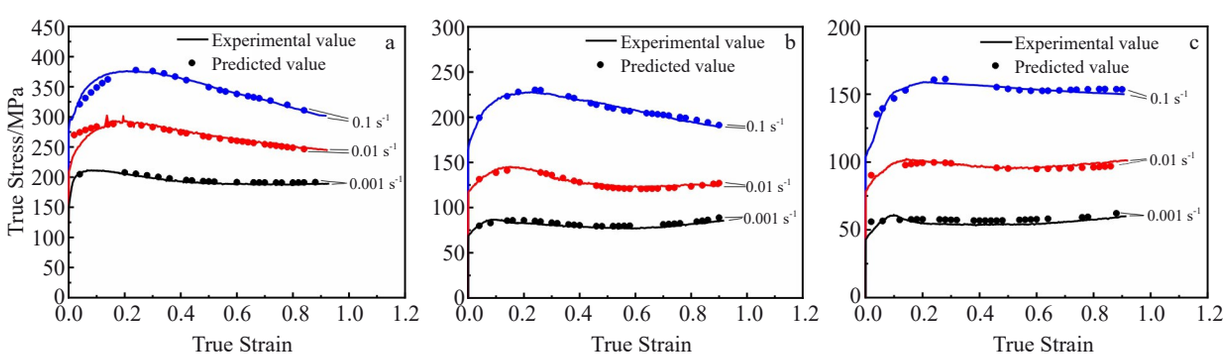

Fig.6 Comparison between true stress values predicted by SVM model and the experimental values of GH738 superalloy at strain rates of 0.001–0.1 s^{-1} and different deformation temperatures: (a) 980 ℃; (b) 1040 ℃; (c) 1100 ℃

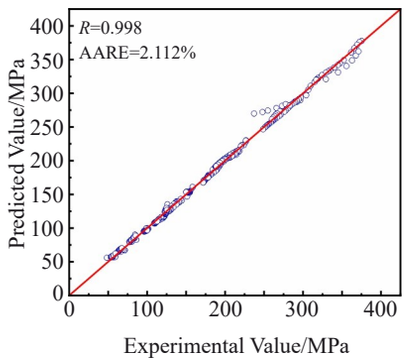

Fig.7 Correlation analysis between the flow stress values predicted by SVM model and the experimental values

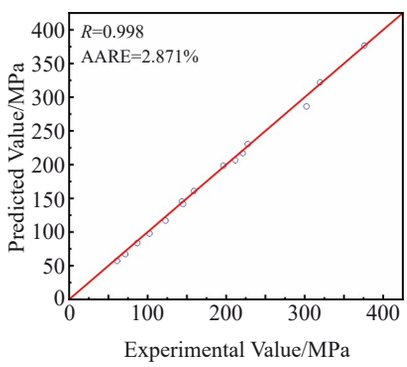

Fig.8 Correlation analysis between the peak stress values predicted by SVM model and the experimental values

by GA-BP model against experimental data. The model achieves exceptional accuracy (AARE=2.103%, R=0.999), with 86.7% of prediction errors less than ±5% from experimental values. Notably, even at critical low-strain regimes (ε<0.1), where RF and SVM models exhibit larger errors, GA-BP model maintains high precision (AARE<2%). This validates its reliability for guiding forging process design, where accurate peak stress prediction is critical for load calculation.

Furthermore, during the early deformation stage, flow stress rises rapidly with the increase in strain, but its growth rate gradually slows down as strain further increases. Eventually, after reaching the peak stress, it begins to decrease gradually until reaching a stable level. The main reason is that at the early stage of deformation, due to the proliferation, cross, and entanglement of dislocations caused by the rapid increase in dislocation density, work hardening dominates, resulting in increased flow stress[69–70]. With the increase in strain, dislocation climbing and cross-slip make dislocations annihilation or rearrangement, offsetting part of the work hardening[71–72]. And the increase in strain is conducive to the occurrence of dynamic recovery or DRX, so the flow stress has been reduced. As the strain continues to increase, when the work hardening and flow softening reach dynamic equilibrium, the true stress-true strain curve gradually enters the steady state stage[73–74].

To quantitatively demonstrate the enhancement from GA optimization, a baseline BP neural network (identical architecture: 3-6-1 nodes) was trained on the same 337 sample dataset. The comparative analysis (Table 3) shows that both accuracy and efficiency have been substantially improved.

This acceleration originates from global optimization of critical parameters via GA: initial weights (w_i), biases (b_i), learning rate (η=0.02), momentum coefficient (α=0.9), and hidden neurons (optimized to 6 neurous). The systematic parameter tuning eliminates local minima stagnation and enhances generalization capability, particularly in low-strain regimes, where AARE of BP reaches 8.72%, compared with only 1.92% of AARE for the GA-BP model.

The performance gap is particularly pronounced in peak stress prediction, where BP model exhibits substantially higher errors than GA-BP model—quantified by the relative error (RE) metric defined as follows[75]:

$$\mathrm{RE}_i = \frac{E_i - P_i}{E_i} \times 100\% \quad (14)$$

where E_i is the experimental value of true stress, and P_i is the predicted value. For peak stress, GA-BP model achieves exceptional accuracy (R=0.999, AARE=2.103%), while BP model demonstrates significantly inferior predictive capability (R=0.986, AARE=5.271%), as shown in Fig. 12. This quantitative discrepancy is further evidenced across testing conditions: GA-BP model maintains exceptional consistency with maximum RE≤7.134% for all 15 peak stress predictions (Fig. 8), whereas BP model shows significant deviations (RE>11.650%) under critical low-temperature conditions (980 °C/0.01 s^{-1}). The marked reduction in prediction error

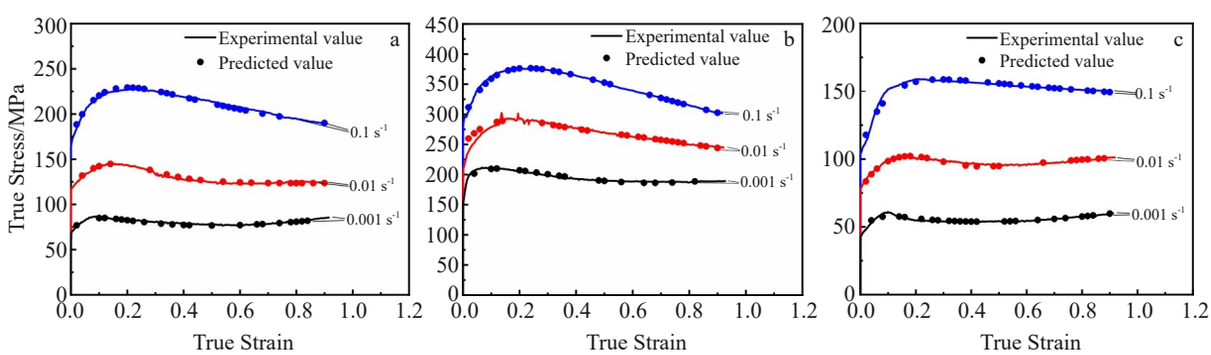

Fig.9 Comparison between true stress values predicted by GA-BP model and the experimental values of GH738 superalloy at strain rates of 0.001–0.1 s^{-1} and different deformation temperatures: (a) 980 °C; (b) 1040 °C; (c) 1100 °C

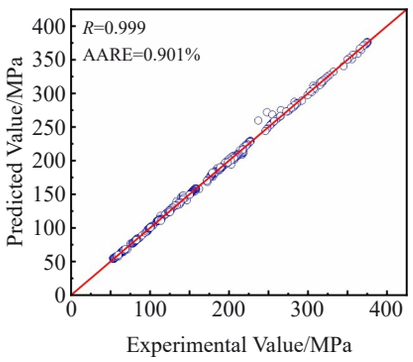

Fig.10 Correlation analysis between the flow stress values predicted by GA-BP model and the experimental values

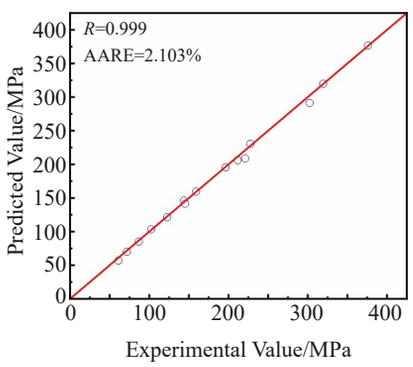

Fig.11 Correlation analysis between the peak stress values predicted by GA-BP model and the experimental values

Table 3 Performance comparison between GA-BP and BP models

Performance metric	BP model	GA-BP model	Improvement
R^2 (training)	0.988	0.999	+1.1%
R^2 (testing)	0.980	0.999	+1.9%
AARE (testing)	4.997%	0.901%	−82.0%
Convergence epoch	150±25	50±10	+67%

Note: the improvement represent the increment of GA-BP model over the BP model.

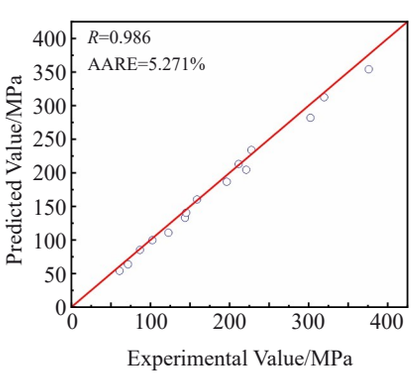

Fig.12 Correlation analysis between the peak stress values predicted by BP model and the experimental values

underscores superiority of GA-BP model in forging load calculations, where accurate peak stress estimation is paramount for optimal press tonnage selection.

4 Comparative Analysis of Prediction Accuracy of Three Constitutive Relationship Models

4.1 Algorithmic origin of reduced strain sensitivity

To quantitatively investigate the source of the relatively large prediction errors exhibited by RF model in the small strain regime (ε<0.1), as shown in Fig.3, shapley additive explanation (SHAP) analysis[76] was applied to assess the differential contributions of the input features (strain ε, strain rate $\dot{\varepsilon}$, and deformation temperature T), as shown in Fig. 13. The mean absolute SHAP values ($|\phi|$) calculated within the critical strain range of $\varepsilon=0.05-0.1$ reveal a significant imbalance in feature influence: strain ε exhibits the weakest contribution ($|\phi|$ =8.2 MPa), substantially lower than deformation temperature T ($|\phi|$ =32.5 MPa) and strain rate $\dot{\varepsilon}$ ($|\phi|$ = 28.7 MPa). This hierarchy of feature importance directly aligns with the inherent characteristics of tree-based algorithms like RF model. Decision trees preferentially use high-variance features for node splitting to maximize information gain[77,21], whereas the restricted variation within the small-strain data ($\Delta\varepsilon$<0.05) provides insufficient information gain to trigger effective splits based on strain. Consequently, RF model demonstrates reduced sensitivity to variations at low strains, correlating directly with the observed prediction deviations (maximum RE of −85.2% at ε<0.1, Fig. 3). This identified algorithmic restriction—distinct from the nonlinear function approximation strengths of models like SVM and GA-BP—provides a more fundamental explanation for the performance gap of RF model during the early deformation stages than the initial qualitative attribution to sample size constraints.

4.2 Performance benchmarking of BP neural network

To evaluate the baseline performance of the unoptimized BP neural network, the independent BP model (with identical 3-6-1 architecture) was benchmarked alongside the established RF, SVM, and GA-BP models. As summarized in Table 4, BP model achieves moderate accuracy (testing AARE=4.997%, R^2=0.980), significantly outperforming RF model (AARE=14.587%, R^2= 0.921) but underperforming relative to SVM (AARE=2.112%, R^2=0.998) and GA-BP (AARE=0.901%, R^2=0.999) models.

4.3 Experimental validation for industrial implementation

The experimental validation of peak stress predictions (Fig.5,

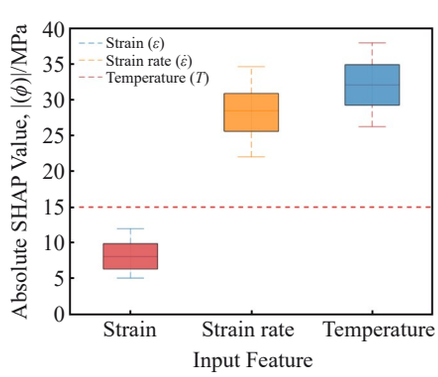

Fig.13 SHAP value distribution in small-strain regime of ε=0.05–0.1

Table 4 Comparation of performance metrics of constitutive models

Performance metric	RF model	BP model	SVM model	GA-BP model
AARE/% (testing)	14.587	4.997	2.112	0.901
R^2 (testing)	0.921	0.980	0.998	0.999

Fig. 8, and Fig. 11) conclusively demonstrates the practical applicability of the developed models. While RF model shows restricted accuracy (AARE=14.587%), SVM and GA-BP models achieve high prediction fidelity (AARE≤2.112%), meeting industrial requirements for deformation resistance estimation (±15% error tolerance). Particularly, near-perfect alignment between peak stress predicted by GA-BP model and experimental peak stresses (R=0.999) confirms its potential to replace physical experiments for flow stress characterization in GH738 superalloy forging simulations.

In summary, AARE values of RF, SVM, and GA-BP constitutive relationship models are 14.587%, 2.112% and 0.901%, respectively, indicating that the prediction accuracy of SVM and GA-BP models is significantly higher than that of RF model. Fig. 14 shows the comparison of AARE values of RF, SVM, and GA-BP models under different deformation conditions. As can be seen from Fig.14, AARE values of SVM and GA-BP models are always lower than that of RF model under all deformation conditions. It can also be seen from Fig. 14 that the prediction error of RF model varies greatly with deformation conditions, while the prediction error of SVM and GA-BP models is relatively stable. For example, the prediction error of RF model under the strain rate of 0.001 s^{-1} (Fig. 14a) and the deformation temperature of 1100 °C (Fig. 14b) is obviously larger than that under other strain rates and deformation temperatures. Meanwhile, with the increase in strain, the prediction error of RF model shows obvious fluctuations, and its AARE gradually decreases when the strain is greater than 0.5 (Fig. 14c). This is because RF model is not sensitive to the change of flow stress at small strain under restricted sample conditions. With the gradual increase in strain, RF model can capture the change characteristics of true stress-true strain curve, making the gradual decrease in prediction error.

In order to further compare the prediction accuracy of RF, SVM, and GA-BP constitutive relationship models, the RE_i of the three models is calculated according to Eq. (14).

RE distribution of RF, SVM, and GA-BP constitutive relationship models is shown in Fig. 15. The values listed at the top represent the percentages of the number of predicted samples within a specific RE range in the total number of predicted samples, and the total number of predicted samples is 338. RE range of RF, SVM, and GA-BP models is [−85.157%, 19.440%], [−15.915%, 6.026%], and [−9.603%, 4.257%], respectively. It can be seen that RE range of RF model is the largest, followed by SVM model; RE range of GA-BP model is the smallest, and its maximum error is not more than ±10%. At the same time, according to Fig. 15, the percentage of RE in the predicted value of RF model within ±10% is only 49.408%. While the percentage of RE within ±10% of SVM model is 99.408%, and the percentage of the RE within ±5% is still as high as 96.745%. Compared with SVM model, the prediction accuracy of GA-BP model is further improved, and the proportion of RE within ±5% of the predicted value is as high as 99.112%.

According to the above prediction accuracy comparison analysis, RF model has poor prediction ability for the flow stress behavior of GH738 superalloy, while the prediction ability of the SVM and GA-BP models is significantly improved, and both of them can accurately predict the flow stress behavior of GH738 superalloy. Therefore, in practical engineering applications, SVM and GA-BP models are feasible, and can basically meet the accuracy requirements of RE (within ±10%). In conclusion, GA-BP and SVM constitutive relationship models can accurately predict the flow stress behavior of GH738 superalloy, which can provide theoretical basis for calculating the deformation resistance and forging tonnage under different deformation conditions, as well as for optimizing the forging process design. It can also provide accurate and reliable flow stress basic data for numerical simulation of the forging process of GH738 superalloy.

4.4 Numerical simulation validation and implications for forging process design

Finite element simulations of GH738 superalloy during compression were performed in Abaqus/Explicit to validate the engineering practicality of the constitutive models. GA-BP

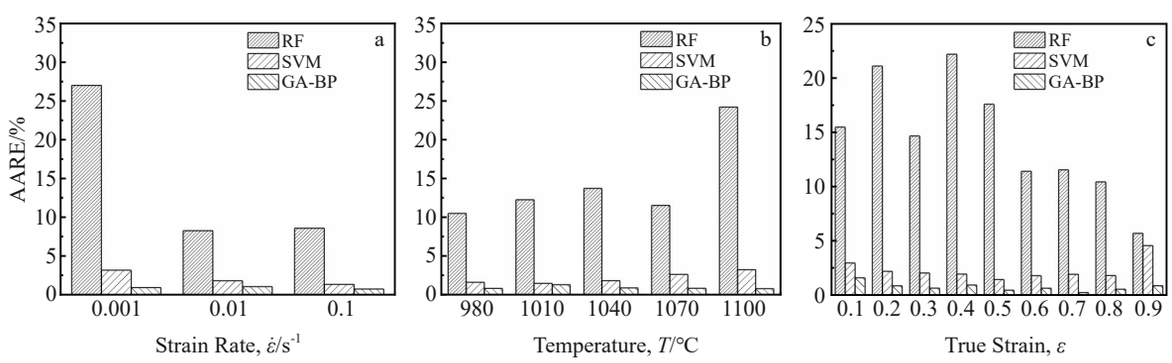

Fig.14 AARE comparison of RF, SVM, and GA-BP constitutive relationship models under different conditions: (a) strain rate; (b) temperature; (c) true strain

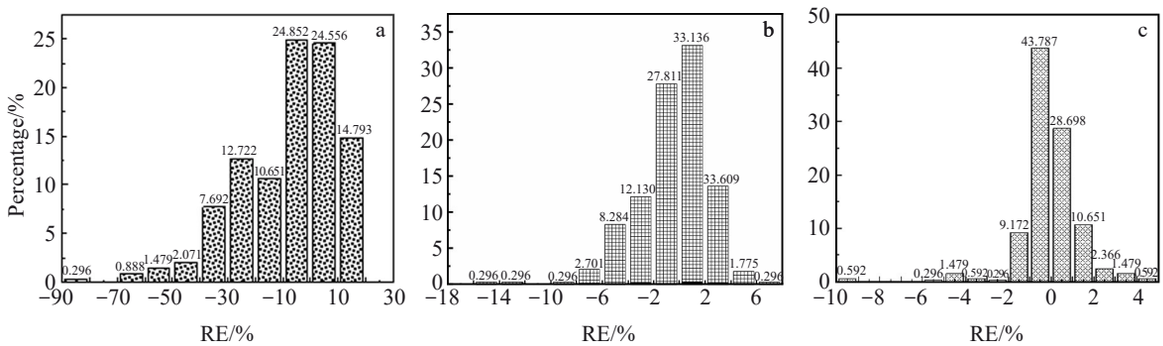

Fig.15 Comparison of RE of RF (a), SVM (b), and GA-BP (c) constitutive relationship models

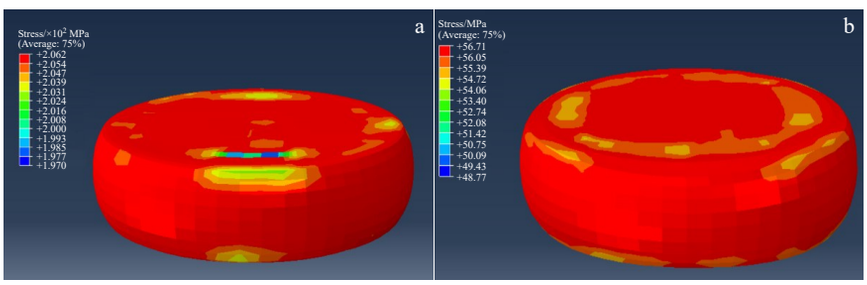

Fig.16 Simulation diagrams of stress distribution predicted by GA-BP model at different conditions: (a) 980 ℃, 0.001 s^{-1}; (b) 1100 ℃, 0.001 s^{-1}

model—selected for its superior prediction accuracy (AARE= 0.901%) —provides temperature-dependent flow stress data. Simulations employed a Φ8 mm×12 mm cylindrical sample (35 000 C3D8R elements, mesh sensitivity validated) under isothermal conditions: temperature of 980/1100±5 °C, constant strain rate of 0.001 s^{-1}, and friction factor of μ=0.3[6]. Stress contours (Fig.16) reveal two critical phenomena.

(1) At 1100 °C, significant thermal softening is observed, with a 72.5% decrease in peak stress (from 206.2 MPa to 56.7 MPa) relative to that at 980 °C, which is consistent with experimental trends.

(2) Characteristic stress heterogeneity with concentrations (>90% peak stress) near die-contact surfaces is consistent with forging defect zones[78]. Validation against GA-BP predictions shows exceptional agreement, with peak stress errors<2.1% at both temperatures. These results demonstrate direct industrial utility. The predicted peak load (1.82 MN at 980 °C) informs press tonnage selection (≥2000 t), while the quantified strain inhomogeneity factor of 0.38 at 1100 °C infers preformance optimization to mitigate defects. This establishes a robust ML-finite element method framework for GH738 superalloy forging process design.

Beyond statistical metrics, significant prediction errors in low-strain regimes (ε<0.1) exhibited by RF and SVM models critically impact forging process design. First, deformation load calculations are highly sensitive to low-strain behavior. Underestimations greater than 15% at ε=0.05, as observed in RF model, result in 25%–32% errors in predicted peak forging load[78–80], directly compromising press tonnage selection. An et al[81] calibrated the strength parameters in the low strain zone of the ceramic JH-2 model through the chaotic optimization algorithm, reducing the prediction error of impact load from >4% to <1%. Second, weak strain sensitivity of RF model ($|\phi|$=8.2 MPa at ε<0.1) in Fig. 8 fundamentally undermines DRX onset prediction. Combined with flow stress errors exceeding 12%, this disrupts DRX kinetics by 25%–40%[82], as inaccurate constitutive models impair microstructure evolution analysis. Third, inaccuracies in the stress state at grain boundaries, where curvature, atomic-scale steps, and lattice distortions govern defect nucleation[83], increase forging defect risks, particularly in aviation components that require costly rework. To mitigate these impacts, two practical recommendations are provided: (1) prioritizing GA-BP model for low-strain region modeling, and (2) imple-menting hybrid GA-BP (ε<0.2)/SVM model to balance accuracy and computational efficiency.

5 Conclusions

1) The flow stress of GH738 superalloy increases with the decrease in deformation temperature and the increase in strain rate. Under the conditions of 980–1100 °C/0.001 s^{-1}, 1010–1100 °C/0.01 s^{-1}, and 1100 °C/0.1 s^{-1}, the flow stress curve presents the characteristics of steady flow. Under the conditions of 980 °C/0.01 s^{-1} and 980–1070 °C/0.1 s^{-1}, the flow stress curve presents the characteristics of flow softening.

2) Among the three constitutive relationship models, GA-BP model has the highest prediction accuracy for the flow stress of GH738 superalloy, and its correlation coefficient R and AARE are 0.999 and 0.901%, respectively. The prediction accuracy of SVM model is the second highest, with R and AARE of 0.998 and 2.112%, respectively. The prediction accuracy of RF model is the worst, with R and AARE of 0.921 and 14.587%, respectively.

3) GA-BP and SVM constitutive relationship models can

accurately predict the flow stress behavior of GH738 superalloy, which can provide theoretical basis for calculating the deformation resistance and forging tonnage under different deformation conditions, as well as for optimizing the forging process design. It can also provide accurate and reliable flow stress basic data for numerical simulation of the forging process of GH738 superalloy.

References

1 Qu J L, Bi Z N, Du J H *et al. Journal of Iron and Steel Research International*[J], 2011, 18(10): 59
2 Shi Z X, Yan X F, Duan C H *et al. Journal of Iron and Steel Research International*[J], 2017, 24(6): 625
3 Wang L, Yang G, Lei T *et al. Journal of Iron and Steel Research International*[J], 2015, 22(11): 1043
4 Yi D Q, Li D, Liu H Q *et al. Journal of Iron and Steel Research International*[J], 2007, 14(5): 1
5 Gu Y L, Tao C H, He Y H. *Journal of Iron and Steel Research International*[J], 2010, 17(6): 74
6 Sui F L, Chen L Q, Liu X H *et al. Journal of Iron and Steel Research International*[J], 2009, 16(5): 43
7 Chen X M, Nie L Y, Hu H W *et al. Materials Today Communications*[J], 2022, 32: 103855
8 Chen X M, Nie L Y, Hu H W *et al. Materials Today Communications*[J], 2023, 35: 105612
9 Jia L, Cui H, Yang S F *et al. Journal of Materials Research and Technology*[J], 2023, 26: 6652
10 Liu Z L, Ren S, Liu W *et al. Transactions of Nonferrous Metals Society of China*[J], 2023, 33(8): 2577
11 Zhang Kaiming, Lu Shiqiang, Jiangfeng Jiancong *et al. Rare Metal Materials and Engineering*[J], 2023, 52(8): 2835 (in Chinese)
12 Lu C Y, Shi J, Wang J. *Materials Characterization*[J], 2021, 181: 111455
13 Chen D D, Lin Y C, Zhou Y *et al. Journal of Alloys and Compounds*[J], 2017, 708: 938
14 Smirnov A, Kanakin V, Konovalov A. *Applied Sciences*[J], 2023, 13(2): 1
15 Bock F E, Aydin R C, Cyron C J *et al. Frontiers in Materials*[J], 2019, 6: 1
16 Rong Q Y, Wei H, Huang X Y *et al. Composites Science and Technology*[J], 2019, 184: 107861
17 Ding S L, Gao S, Jiang X *et al. Materials Today Communications*[J], 2025, 42: 111230
18 Xiao Y Z H, Deng Y C, An Y X *et al. Materials Today Communications*[J], 2024, 40: 109881
19 Poluru S, Jaimin A, Kotkunde N R *et al. Materials & Design*[J], 2025, 254: 114035
20 Qiao L, Inoue J, Zhu J C. *Journal of Materials Research and Technology*[J], 2024, 29: 353
21 Breiman L. *Machine Learning*[J], 2001, 45: 5
22 Khajavi H, Rastgoo A. *Sustainable Cities and Society*[J], 2023, 93: 104503
23 Mcelfresh C, Roberts C, He S C *et al. Computational Materials Science*[J], 2022, 208: 111267
24 Aghaaminiha M, Mehrani R, Colahan M *et al. Corrosion Science*[J], 2021, 193: 109904
25 Sun Z G, Wang G T, Li P F *et al. Expert Systems with Applications, Part B*[J], 2024, 237: 121549
26 Zhang R, Wang J, Jiang N *et al. Information Sciences*[J], 2023, 635: 25
27 Alfaleh A, Khedher N B, Eldin S M *et al. Energy Reports*[J], 2023, 10: 1259
28 Li Y D, Mi G B, Li P J *et al. Chinese Journal of Engineering*[J], 2022, 44(6): 1036
29 Limbadri K, Pankaj W, Suresh K *et al. Journal of Materials Engineering and Performance*[J], 2022, 32(2): 462
30 Desu R K, Guntuku S C, Aditya B *et al. Procedia Materials Science*[J], 2014, 6: 368
31 Lian P L, Liu H, Wang X *et al. Measurement*[J], 2020, 165: 108109
32 Chen W N, Li S J, Bhandari K S *et al. International Journal of Mechanical Sciences*[J], 2023, 244: 108077
33 Zhu Y L, Cao Y, Liu C J *et al. Materials Today Communications*[J], 2020, 25: 101329
34 Chu L H, Wang L, Li H Y *et al. Journal of Netshape Forming Engineering*[J], 2017, 9(6): 125
35 Wen D X, Yue T Y, Xiong Y B *et al. Materials Science and Engineering A*[J], 2021, 803: 140491
36 James G, Witten D, Hastie T *et al. An Introduction to Statistical Learning: with Applications in R*[M]. New York: Springer, 2013
37 Zhou J, Dai Y, Tao M *et al. Results in Engineering*[J], 2023, 17: 100892
38 Zhou Zhihua. *Machine Learning*[M]. Beijing: Tsinghua University Press, 2016 (in Chinese)
39 Wang B, Qiu W T, Hu X *et al. Applied Soft Computing*[J], 2024, 156: 111506
40 Cortes C, Vapnik V. *Machine Learning*[J], 1995, 20: 273
41 Suykens J, Vandewalle J. *Neural Processing Letters*[J], 1999, 9: 293
42 Li Hang. *Statistical Learning Methods*[M]. Beijing: Tsinghua University Press, 2012 (in Chinese)
43 Vapnik V N. *The Nature of Statistical Learning Theory*[M]. New York: Springer, 1995
44 Boser B E, Guyon I M, Vapnik V N. *Proceedings of the Fifth Annual Workshop on Computational Learning Theory*[C]. New York: Association for Computing Machinery, 1992: 144
45 Hsu C W, Chang C C, Lin C J. *Journal of Machine Learning Research*[J], 2016, 17(12): 1
46 Wang Y T, Li J L, Yuan K F *et al. Journal of Materials Engineering*[J], 2022, 50(6): 170
47 Huang S Z, Jiang C W, Tian Z W *et al. Materials Today Communications*[J], 2023, 35: 106149
48 Singh D, Singh B. *Applied Soft Computing Part B*[J], 2020, 97: 105524
49 Murugesan M, Jung D W. *Materials Science Forum*[J], 2020, 977: 163
50 Yang J F. *Physical Communication*[J], 2020, 42: 101
51 Li X W, Wang J H, Ma J X *et al. Journal of Materials Research and Technology*[J], 2023, 24: 1802
52 Goldberg D E. *Genetic Algorithms in Search, Optimization, and Machine Learning*[M]. Reading: Addison-Wesley Publishing

Company, 1989
53 Pei X L, Pei J Q, Hou H *et al. npj Computational Materials*[J], 2025, 11: 27
54 Lypchanskyi O, Śleboda T, Zyguła K *et al. Materials*[J], 2020, 13(16): 3629
55 Jedynak A, Sviridov A, Bambach M *et al. Procedia Manufacturing*[J], 2020, 47: 1149
56 Sahithya K, Balasundar I, Pant P *et al. Materials Science and Engineering A*[J], 2019, 754: 521
57 Zhou H P, Zhang H B, Liu J *et al. Rare Metal Materials and Engineering*[J], 2018, 47(11): 3329
58 Vespa G, Mackenzie L W F, Verma R *et al. Materials Science and Engineering A*[J], 2008, 487(1–2): 243
59 Lu C Y, Wang J, Zhang P. *Journal of Materials Engineering and Performance*[J], 2021, 30(10): 7668
60 Zhang Y, Liu P, Tian B H *et al. Transactions of Nonferrous Metals Society of China*[J], 2013, 23(4): 970
61 Long L, Xia Q, Xiao G *et al. International Journal of Mechanical Sciences*[J], 2021, 191: 106069
62 Tu F, Su X P, Zhang F Y *et al*. *Rare Metals*[J], 2011, 35(3): 388
63 Wang L, Yang G, Lei T *et al. International*[J], 2015, 22(11): 1043
64 Abellan-Garcia J, García-Castaño E, Fernández-Gómez J *et al*. *Materials Today Communications*[J], 2023, 37: 106953
65 Nayan N, Singh G, Narayana Murty S V S *et al*. *Intermetallics*[J], 2021, 131: 107084
66 Qiao L, Inoue J, Zhu J C. *Journal of Materials Research and Technology*[J], 2024, 29: 353
67 Poluru S, Jaimin A, Kotkunde N *et al. Materials & Design*[J], 2025, 254: 114035
68 Dong X M, Xu J, Feng Z X *et al. Journal of Materials Research and Technology*[J], 2024, 29: 2142
69 Li Z Q, Wang D C, Wang L P *et al. Materials Today Communications*[J], 2024, 39: 108626
70 Li X W, Wang J H, Ma J X *et al. Journal of Materials Research and Technology*[J], 2023, 24: 1802
71 Liu Y, Sun P, Wang M *et al. Intermetallics*[J], 2024, 173: 108406
72 Liu T, Cheng X N, Luo R *et al. Materials Science and Engineering A*[J], 2021, 819: 141533
73 Ding B, Cai J, Zhang B *et al. Journal of Plasticity Engineering*[J], 2023, 30(9): 131
74 Fan X G, Zhang Y, Gao P F *et al. Materials Science and Engineering A*[J], 2017, 694: 24
75 Amitava R, Mohammad A, Satyabrata D *et al. Metallurgical and Materials Transactions B*[J], 2019, 50: 1061
76 Wang H X, Duan Z Q, Guo Q W *et al. CMC-Computers, Materials & Continua*[J], 2023, 77: 2
77 Lundberg S M, Lee S I. *The 31st International Conference on Neural Information Processing Systems*[C]. Long Beach: Curran Associates Inc., 2017: 4768
78 Tolvanen J, Leminen V, Tanninen P *et al. Procedia Manufacturing*[J], 2017, 11: 482
79 Bao Lei, Wang Diange, Zhang Changlong *et al. Chinese Materials Science and Technology & Equipment*[J], 2014, 10(1): 3 (in Chinese)
80 Kodippili T, Lambert S, Arami A. *Materials Today Communications*[J], 2022, 31: 103210
81 An R, Wang Y W, Fu Q *et al. International Journal of Impact Engineering*[J], 2023, 172: 104424
82 Mirzadeh H. *Mechanics of Materials*[J], 2015, 85: 66
83 Zhao Q, Zhu Q, Zhang Z *et al. Journal of the Mechanics and Physics of Solids*[J], 2023, 181: 1045

基于机器学习的GH738高温合金流动应力本构关系研究

王双见[1]，王克鲁[1]，鲁翠媛[2]，罗佰乐[1]，徐　兵[3]，周世鑫[3]，王攀智[3]
(1. 南昌航空大学 航空制造工程学院，江西 南昌 330063)
(2. 南昌大学 先进制造学院，江西 南昌 330031)
(3. 贵州航宇科技发展股份有限公司，贵州 贵阳 550081)

摘　要：在变形温度980~1100 ℃、应变速率0.001~0.1 s^{-1}条件下，采用Gleeble 3500热模拟试验机对GH738高温合金进行等温恒应变速率压缩试验，研究了合金的流动应力行为，建立了随机森林、支持向量机和遗传算法优化反向传播网络（GA-BP）3种机器学习型本构关系模型，并对模型预测精度进行了对比分析。结果表明，GH738高温合金的流动应力随变形温度升高和应变速率降低而减小。随机森林、支持向量机和GA-BP本构关系模型的相关系数R分别为0.921、0.998和0.999，平均绝对相对误差分别为14.587%、2.112%和0.901%，说明支持向量机和GA-BP本构关系模型预测精度远高于随机森林模型，它们能较准确地预测GH738高温合金的流动应力行为，可为不同变形条件下的变形抗力和锻造吨位计算提供理论依据，也可为锻造过程数值模拟提供准确、可靠的流动应力数据。

关键词：GH738高温合金；本构关系模型；随机森林；支持向量机；GA-BP网络

作者简介：王双见，男，1998年生，硕士，南昌航空大学航空制造工程学院，江西 南昌 330063，E-mail：884253322@qq.com